## Electronic materials

# One-step chemical bath co-precipitation method to prepare high hydrogen-producing active $Zn_xCd_{1-x}S$ solid solution with adjustable band structure

Lili Lu[1], Yongjin Ma[1], Rui Dong[1], Pengfei Tan[1], Yi Chen[2,*], and Jun Pan[1,*]

[1] *State Key Laboratory for Powder Metallurgy, Central South University, Changsha 410083, P. R. China*
[2] *Hunan Key Laboratory of Water Safety Discharge in Urban and Its Resource Utilization, College of Urban and Environmental Sciences, Hunan University of Technology, Zhuzhou 412007, P. R. China*

## ABSTRACT

A series of $Zn_xCd_{1-x}S$ solid solutions were synthesized through a simple one-step chemical bath co-precipitation route. The microstructure, morphology, composition and optical properties had been thoroughly investigated. The results showed that the as-obtained $Zn_xCd_{1-x}S$ samples exhibited monodisperse spherical feature. These monodisperse $Zn_xCd_{1-x}S$ spheres were composed of a large number of 5–10 nm crystal grains. The chemical composition of the $Zn_xCd_{1-x}S$ solid solutions can be controlled by adjusting the ratio of Zn source to Cd source and the dosage of ammonia solution. Meanwhile, the energy band structure and photocatalytic properties can be optimized. The photocatalysis experiment results revealed that the as-synthesized $Zn_{0.30}Cd_{0.70}S$ sample exhibited optimum water splitting performance. The satisfactory hydrogen evolution rate (HER) of $Zn_{0.30}Cd_{0.70}S$ reached 27.004 mmol $g^{-1}$ $h^{-1}$ even without any cocatalysts, which was more than 48 times that of pure CdS (0.561 mmol $g^{-1}$ $h^{-1}$). This enhancing effect can owe to the balance between light absorption capacity and redox potential caused by the incorporation of Zn in the $Zn_xCd_{1-x}S$ solid solutions.

## Introduction

As human society is constantly evolving, energy crisis and environmental damage problems have become the two major issues that must be solved

immediately [1, 2]. Hydrogen energy, a clean and renewable fuel, has received extensive attention. Since Honda and Fujishima discovered a feasible photoelectrochemical (PEC) method for reducing water to produce hydrogen on the $TiO_2$ electrodes [3], this photocatalytic technology of using solar energy to split water has received widespread attention by researchers. Because this PEC method is a promising green solution for converting solar energy into chemical energy to produce hydrogen,

which is considered to be the most ideal approach to solving both environmental and energy problems [4–7]. Since then, numerous potential semiconductor materials have been used in the practice of PEC water splitting, such as SrTiO$_3$ [8–10], BaTiO$_3$ [10, 11], ZnO [12, 13], CeO$_2$ [14, 15], g-C$_3$N$_4$ [15–18], ZnS [19–21] and CdS [21–24]. However, most of them can only operate in the ultraviolet region, which greatly limits their wide applications. Hence, it is imperative to develop visible light-responsive catalysts that can more effectively use solar energy.

As a typical semiconductor photocatalyst that can respond to visible light, CdS has a small band gap ($E_g$) and a favorable redox potential, which is suitable for photocatalytic water splitting [25]. Unfortunately, the severe recombination process of photogenerated carriers and serious photocorrosion result in low photocatalytic performance and poor cycle stability [23–25], which severely limit the wide application in photocatalytic water splitting. At the same time, CdS has strong toxicity. On the contrary, as another representative of II–VI semiconductor, ZnS has excellent properties complementary to CdS, such as high energy conversion efficiency, good photocatalytic stability, low toxicity and relatively negative reduction potential, although it only works under ultraviolet light. Therefore, the combination of ZnS and CdS should be a viable method to take advantage of the virtues of these two semiconductors and improve their respective defects. Constituted ternary metal sulfides system (Zn$_x$Cd$_{1-x}$S), which can continuously regulate the $E_g$ from about 2.4 eV (CdS) to 3.8 eV (ZnS) by adjusting the content of Zn and Cd ions [26–28], often shows excellent catalytic performance. Up till the present moment, many efforts have been paid to synthesize high-performance Zn$_x$Cd$_{1-x}$S catalysts. For example, Chen et al. had prepared H-ZnCdS rhombic cages, fabricated by vulcanizing the single precursor of ZIF-8 and then performing cation exchange by hydrothermal method at 160 °C [29]. Li et al. had developed a route to directly pyrolyze zinc–cadmium–thiourea complex at 500 °C to obtain high-efficiency Zn$_{1-x}$Cd$_x$S photocatalysts [27]. Zhang et al. used layered porous ZnS nanospheres as a sacrificial template, followed by co-hydrothermal with Cd(Ac)$_2$ at 140 °C to form Zn$_x$Cd$_{1-x}$S double-shell hollow nanospheres [30]. In addition, Xiang et al. used oleylamine as an organic solvent to successfully synthesize sphalerite-type structured Cd$_{1-x}$Zn$_x$S nanocrystals through an organic solution method at 280 °C [31]. From the results, these

Zn$_x$Cd$_{1-x}$S solid solutions obtained through the above strategy showed significantly improved H$_2$ evolution performance compared with pure CdS materials. But, the above-reported synthesis process usually involves complex routes and stringent reaction conditions, such as high temperature, high pressure, multiple precursors or organic solvents. Hence, it is meaningful to open up a simple and gentle route to synthesize Zn$_x$Cd$_{1-x}$S photocatalytic materials and at the same time aim to further improve their hydrogen evolution performance. Among many material synthesis methods, chemical bath method is widely used in the synthesis of various materials because of its simple and convenient operation [32]. The chemical bath method can be carried out at low temperature and normal pressure, and the reaction time is generally short. Therefore, for the consideration of scale production and practical application, this method has obvious advantages. For this reason, we tried to synthesize the Zn$_x$Cd$_{1-x}$S photocatalyst under a mild condition through a simple one-step chemical bath co-precipitation method. To our knowledge, there is no report on the synthesis of monodisperse Zn$_x$Cd$_{1-x}$S nanosphere material for photocatalytic hydrogen evolution by this method.

Here, we successfully synthesized a series of Zn$_x$Cd$_{1-x}$S solid solution materials via a simple chemical bath co-precipitation route without using any organic solvents or templates. These solid solutions obtained by inserting Zn ions into the CdS lattice inherit the advantages of the visible light response of CdS and the high reduction potential of ZnS and improve the problems of severe photocorrosion of CdS and the narrow light response range of ZnS. The resulting photocatalysts were characterized by various methods and applied to water reduction. In addition, we also explored the effect of ammonia solution on the formation of solid solutions.

## Experimental section

### Materials

Zinc nitrate hexahydrate, cadmium nitrate tetrahydrate and thiourea were obtained from Aladdin. Trisodium citrate dihydrate and ammonia solution (NH$_3$·H$_2$O, 25%) were obtained from Sinopharm. All raw materials were of analytical grade. Deionized water from local sources was used as solvent.

## Synthesis of $Zn_xCd_{1-x}S$ and $Zn_xCd_{1-x}S$-n monodisperse spheres

Samples were synthesized using a simple one-step chemical bath co-precipitation method. Typically, to synthesize $Zn_{0.30}Cd_{0.70}S$ ($Zn_{0.30}Cd_{0.70}S$-1) solid solution material, 5 mL of trisodium citrate dihydrate (0.12 M), 7 mL of cadmium nitrate tetrahydrate (0.05 M) and 3 ml of zinc nitrate hexahydrate (0.05 M), 1 mL of ammonium solution (17.03 M), and 4 mL of thiourea (0.5 M) were sequentially poured into a 250-ml three-necked flask containing 100 mL of deionized water every 10 min under continuous magnetic stirring. Then, the reaction system was kept in an oil bath at 80 °C for 3 h. Subsequently, the suspended yellow precipitate was collected and preserved. By appropriately regulating the ratio of Cd source to Zn source (the amount of ammonia solution was 1 ml) or the dosage of ammonia solution (the ratio of Cd source to Zn source was 7 to 3), a series of $Zn_xCd_{1-x}S$ and $Zn_xCd_{1-x}S$-n (the amount of ammonia solution was n ml) solid solution materials can be easily obtained via a similar procedure.

## Characterization

Crystal structure and crystalline quality of all specimens were examined by the powder X-ray diffraction (D/max 2550, Rigaku Corporation) in the $2\theta = 10°–80°$ range. The morphologies and structures were characterized by scanning electron microscope (Nova Nano SEM 230, FEI Electron Optics B.V) and transmission electron microscope (JEM-2100F, Japan Electronics Co. LTD). Microanalysis of energy-dispersive X-ray (EDX) spectrum was also obtained from the above-mentioned scanning electron microscope. Element mapping is performed on transmission electron microscope (Titan G260-300). The surface element information was collected from X-ray photoelectron spectroscopy (K-Alpha 1063, Thermo Fisher). The UV–Vis diffuse absorption spectra were gained from a UV–Vis spectrometer (Evolution 220, Thermo Fisher Scientific) to reveal the optical physical properties.

## Photocatalytic tests

The catalytic ability of all synthesized solid solution catalysts was evaluated by reducing water under simulated sunlight irradiation. In a representative catalytic hydrogen production reaction, $Zn_xCd_{1-x}S$ photocatalyst (10 mg) and sacrificial reagents (0.035 mol of $Na_2S$ and 0.025 mol of $Na_2SO_3$) were ultrasonically dispersed in a glass reactor containing 0.1 L of deionized water. Then, the reactor was connected to a vacuum system so that the entire reaction process was performed in a vacuum state. The above reactor was irradiated under a 300 W Xe lamp and kept at 5 °C by circulating condensed water. The amount of hydrogen produced by the reaction system was analyzed by a gas chromatograph every hour.

## Electrochemical analysis

The CHI 660E electrochemical workstation was used to reveal the PEC properties of the prepared catalysts, including Mott–Schottky curves, electrochemical impedance spectroscopy (EIS), and transient-state photocurrent response. A standard three-electrode system was adopted. Saturated Ag/AgCl electrode was acted as reference electrode, while platinum foil was used as counter electrode. Working electrodes were obtained as follows: First, catalyst specimen (5 mg) was ultrasonically dispersed in the glycol solution (2 mL) and kept under magnetic stirring for 24 h; then, the catalyst slurry (100ul) was evenly coated on the fluorine-doped tin oxide (FTO) glass (10 mm × 10 mm); finally, the working electrodes can be obtained by completely evaporating the solvent. The EIS test was performed in the frequency range of 1000 kHz–0.1 Hz with an amplitude of 5 mV. Under simulated sunlight, transient photocurrent was collected for a period of 40 s. The Mott–Schottky curves were recorded at a frequency of 500 Hz and an amplitude of 50 mV under the dark condition. The applied voltage varies from − 1.5 V to 1.0 V.

## Results and discussion

Powder X-ray diffraction (XRD) was used to analyze the crystal structure and crystalline quality of as-synthesized $Zn_xCd_{1-x}S$ products (Fig. 1a). As seen from Fig. 1a, black line, the XRD pattern of pure CdS sample can be assigned to the hexagonal wurtzite structure, which could be indexed as the standard card (JCPDS no. 41–1049). The three diffraction peaks located at 24.8°, 26.5° and 28.2° corresponded to (100), (002) and (101) planes, respectively. It was not

difficult to find that as the value of x increased, the pattern peaks of $Zn_xCd_{1-x}S$ shifted to a large angle. This phenomenon indicated that zinc ions had been incorporated into the crystal lattice of CdS crystals to form a solid solution, while reducing the lattice distance of CdS crystals [30, 33, 34]. What's more, the two diffraction peaks near 24.8° and 28.2° were not particularly noticeable due to poor crystallization performance induced by low temperature reaction and the increase in zinc composition. And the absence of additional phases meant that the synthetic material was a single phase.

The XRD patterns of $Zn_xCd_{1-x}S$-n (attained with the addition of n mL $NH_3·H_2O$, while the ratio of Cd source to Zn source was 7 to 3 in the initial reaction solution) are revealed in Fig. 1b. The XRD peaks not only shifted to left side with the increase in the n value, but also the two diffraction peaks near 24.8° and 28.2° gradually became prominent. The shift of the diffraction peaks to the left meant that the cadmium content had increased in the solid solution. At the same time, the observation of the two XRD peaks near 24.8° and 28.2° showed the improvement in the crystallinity of the obtained material. These phenomena strongly proved that the dosage of ammonia solution not only adjusted the composition of $Zn_xCd_{1-x}S$, but also affected the crystallinity.

To reveal the optical properties of synthetic materials, solid UV–Vis diffuse reflectance spectra (DRS) are given in Fig. 2a. Obviously, as the zinc content increased, the absorption edges of all specimens showed successive blue shift one after another instead of two-stage absorption, which strongly confirmed the formation of solid solutions. The result was consistent with the XRD result. This also agreed with other studies [27, 28, 33, 34]. To further reveal the changes in the optical properties, the $E_g$ energy values corresponding to $Zn_xCd_{1-x}S$ (x = 0, 0.14, 0.30,

and 0.46) materials were determined by Kubelka–Munk method [20, 27, 35]. As seen from Fig. 2b, the estimated $E_g$ values were 2.29, 2.39, 2.48 and 2.56 eV, respectively. It showed that the incorporated Zn ions in the CdS crystal increased the $E_g$, thereby reducing the incident light absorption range of $Zn_xCd_{1-x}S$ catalysts.

To achieve a further insight of the energy band structure about the as-synthesized $Zn_xCd_{1-x}S$ materials, we performed Mott–Schottky measurements [36]. The Mot–Schottky curves (Fig. 2c) showed that the reduction potential of all solid solutions had a negative correlation with x value. A larger zinc content results in a more negative conduction band (CB) edge, and a more negative CB edge means stronger reducing ability, which is helpful to strengthen the activity of reduction to produce $H_2$ [28, 30]. From the results of Mott–Schottky measurements and Kubelka–Munk plots, the band structure information of $Zn_xCd_{1-x}S$ samples can be obtained in detail, as shown in Fig. 2d and Table 1.

The morphologies and structures of the synthetic products with different metal compositions were detected by scanning and transmission electron microscopy (SEM and TEM). As seen from Fig. 3a–b and Fig. 4a–f, all prepared $Zn_xCd_{1-x}S$ samples were uniformly monodisperse nanospheres. The surface of $Zn_xCd_{1-x}S$ nanospheres tended to be regular as Zn ions were continuously incorporated into the CdS crystal lattice. TEM micrographs are shown in Fig. 3b and Fig. 4d–f, indicating that the rough surface of the nanospheres is composed of numerous small-sized nanocrystals. As shown in Fig. 3c, the high-resolution TEM micrograph of $Zn_{0.30}Cd_{0.70}S$ revealed that the grain size was about 5–10 nm, which is supposed to contribute to a significant increase in catalytic performance [29]. The d spacing of lattice fringes of the random nanoparticle was measured to be 3.36 Å and

**Figure 1** **a** XRD patterns of $Zn_xCd_{1-x}S$ samples; **b** XRD patterns of $Zn_xCd_{1-x}S$-n samples.
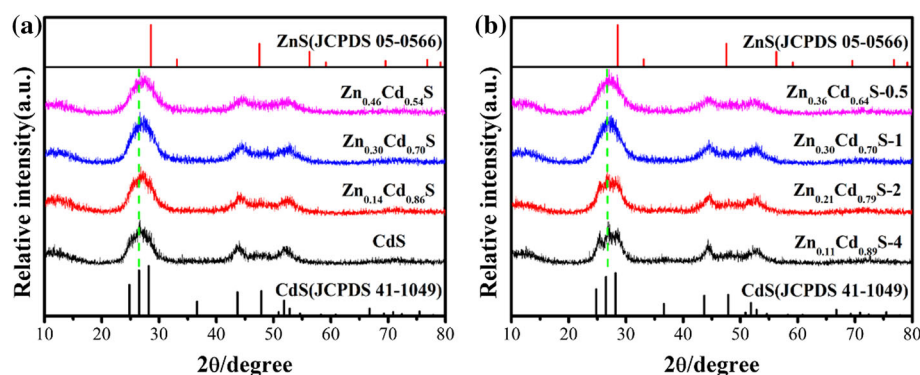
**Figure 2** **a** UV–Vis DRS;
**b** Kubelka–Munk plots;
**c** Mott–Schottky curves and
**d** the conduction band and
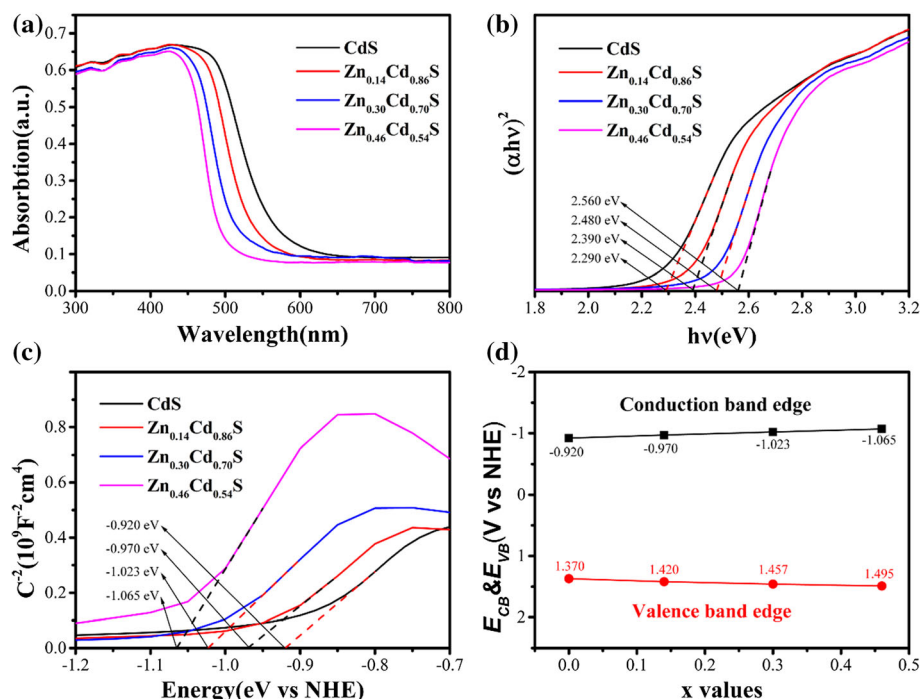valence band (VB) potentials
of various $Zn_xCd_{1-x}S$ samples.



**Table 1** EDX results of all products and the corresponding band structure information

| Sample | Zn:Cd (Atomic ratio) | $E_g$ (eV) | $E_{CB}$ (eV) | $E_{VB}$ (eV) |
|---|---|---|---|---|
| CdS | 0:1 | 2.290 | $-$ 0.920 | 1.370 |
| $Zn_{0.14}Cd_{0.86}S$ | 0.140:0.860 | 2.390 | $-$ 0.970 | 1.420 |
| $Zn_{0.30}Cd_{0.70}S$ | 0.303:0.697 | 2.480 | $-$ 1.023 | 1.457 |
| $Zn_{0.46}Cd_{0.54}S$ | 0.458:0.542 | 2.560 | $-$ 1.065 | 1.495 |
| $Zn_{0.36}Cd_{0.64}S$-0.5 | 0.362:0.638 | – | – | – |
| $Zn_{0.21}Cd_{0.79}S$-2 | 0.210:0.790 | – | – | – |
| $Zn_{0.11}Cd_{0.89}S$-4 | 0.111:0.889 | – | – | – |

2.07 Å corresponding to the (002) and (110) planes of the $Zn_{0.30}Cd_{0.70}S$ solid solution, respectively, which matched the XRD results. The EDX spectrum (Fig. 3d) confirmed that the materials we prepared were composed of cadmium, zinc and sulfur elements. And the elemental compositions of all samples were determined, as shown in Table 1. As shown in Fig. 3e–h, the element mapping images were given, which confirmed that Zn, Cd and S elements were uniformly distributed throughout the as-prepared monodisperse nanospheres.

As shown in Fig. 4g–i, the morphologies and size distribution of $Zn_xCd_{1-x}S$-n specimens were displayed at different ammonia levels. It was very clear that the dosage of ammonia only affected the size of the sample, but the spherical feature did not change significantly. With the increase in ammonia solution,

the sample size increased from approximately 80 to 148 nm. At the same time, the EDX test results (Table 1) showed changes in the composition of the prepared samples, which confirmed the conclusion of XRD. In the case where the Zn/Cd precursor solution ratio remained unchanged, proper adjustment of the dosage of ammonia solution could change the composition of the final products. With the increase in the dosage of ammonia solution, thiourea was accelerated to decompose to produce $S^{2-}$, which significantly affected the nucleation and growth process, leading to accelerated precipitation reaction. In this process, on the one hand, the grain growth was promoted and the grain size became larger, which led to an increase in crystallinity; on the other hand, the size of the solid solution spheres increased with the acceleration of the precipitation reaction. As we all
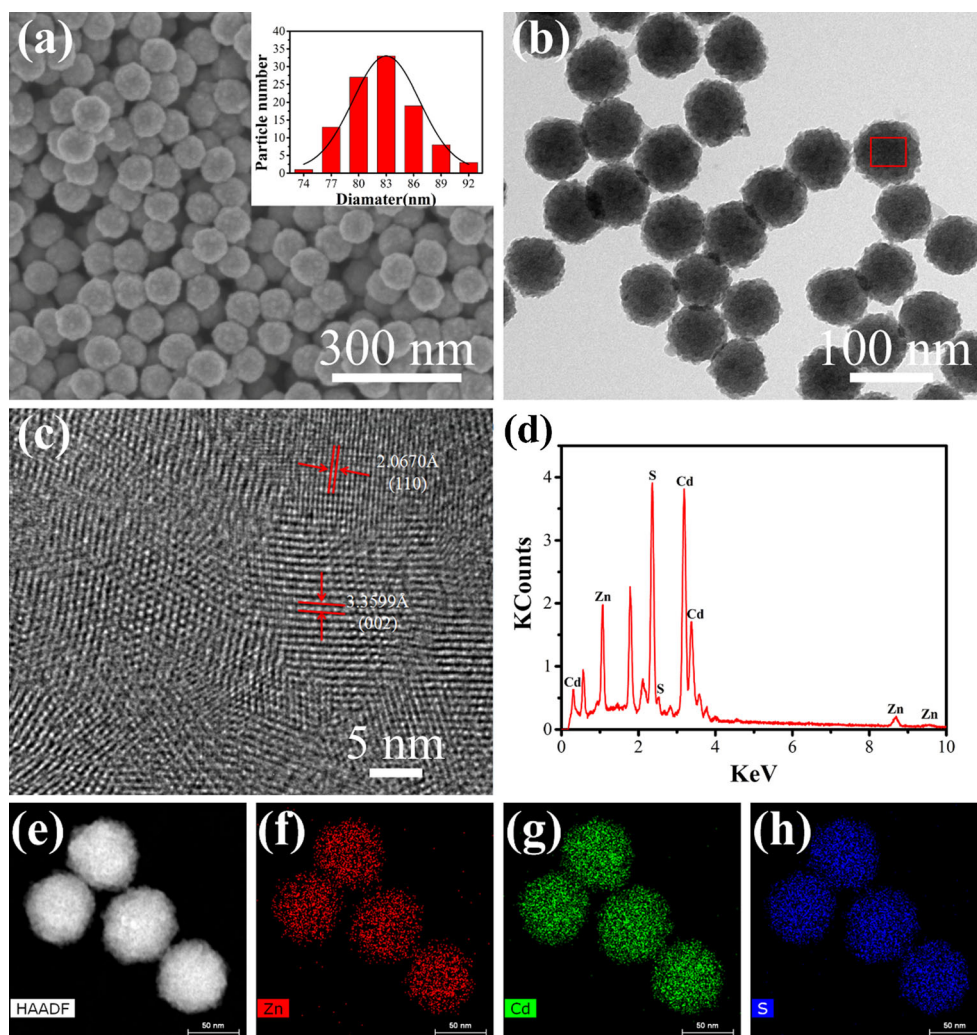
**Figure 3** Typical SEM and size distribution curve **a**, TEM **b**, high-resolution TEM **c** images, EDX spectrum **d**, and element mapping images **e–h** of $Zn_{0.30}Cd_{0.70}S$ nanospheres.

know, under the same conditions, the solubility constant of ZnS is significantly higher than that of CdS. Therefore, CdS is easier to deposit. So, during the co-precipitation process, $Cd^{2+}$ ions were obviously in a favorable position during the reaction with $S^{2-}$ ions, which led to a slight increase in the Cd content in the resulting solid solution [37].

The surface element information of photocatalysts was detected by X-ray photoelectron spectroscopy (XPS). Figure 5a is XPS full spectra of the corresponding $Zn_xCd_{1-x}S$ samples. Obviously, the XPS full spectrum of CdS was mainly composed of the diffraction peaks of cadmium and sulfur. In addition, XPS peaks of cadmium, zinc and sulfur can be discovered in the other three $Zn_xCd_{1-x}S$ samples. High-resolution XPS spectra did prove the presence of

cadmium, zinc and sulfur (Fig. 5b–d). The results were completely consistent with the EDX test. As the zinc content increased, the spectral intensity of Zn 2p gradually increased (Fig. 5c), while the spectral intensity of Cd decreased slightly (Fig. 5b), denoting that the relative content of zinc and cadmium can be easily adjusted [38]. The S 2p spectra of all specimens showed similar peak intensities (Fig. 5d). As the zinc content increased, the binding energy of S 2p gradually increased from 161.28 eV of CdS to 161.78 eV of $Zn_{0.46}Cd_{0.54}S$, indicating that a large number of more stable ZnS chemical bonds were formed in $Zn_xCd_{1-x}S$ samples [38]. At the same time, the binding energy of Cd $3d_{5/2}$ and Cd $3d_{3/2}$ increased from 405.14 eV and 411.04 eV to 405.36 eV and 412.09 eV. Continuous
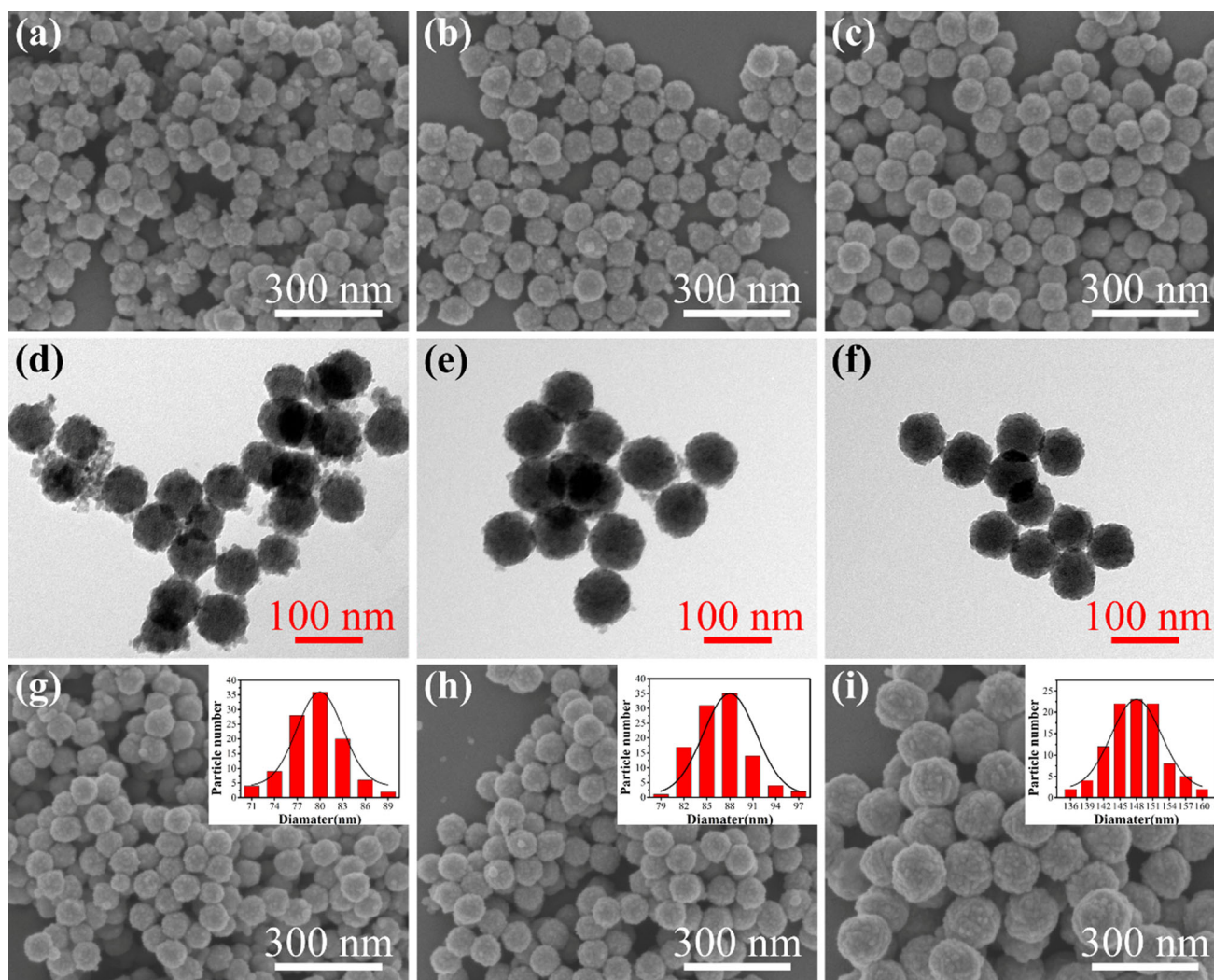
**Figure 4** SEM and TEM images of CdS **a, d**, $Zn_{0.14}Cd_{0.86}S$ **b, e**, $Zn_{0.46}Cd_{0.54}S$ **c, f**; SEM images and size distribution curve of $Zn_{0.11}Cd_{0.89}S$-0.5 **g**, $Zn_{0.21}Cd_{0.79}S$-2 **h** and $Zn_{0.36}Cd_{0.64}S$-4 **i**.

changes in the binding energy also suggested the formation of solid solutions.

The catalytic performance of synthetic $Zn_xCd_{1-x}S$ specimens was evaluated toward $H_2$ evolution without the assistance of any cocatalyst. Mixed aqueous solutions containing 0.25 M $SO_3^{2-}$ and 0.35 M $S^{2-}$ were used as sacrificial agents system to prevent photocorrosion of the sulfide photocatalyst. As seen from Fig. 6a, the hydrogen evolution rate (HER) of pure CdS under simulated sunlight irradiation was negligible (0.561 mmol $g^{-1}$ $h^{-1}$). Surprisingly, with the embedding of Zn ions, the HER of $Zn_xCd_{1-x}S$ increased dramatically. As for $Zn_{0.3}Cd_{0.7}S$, the HER reached a peak value of 27.004 mmol $g^{-1}$ $h^{-1}$, which was about 48 times the HER of pure CdS. However, with the further increase

in zinc content, the performance of $Zn_{0.46}Cd_{0.64}S$ catalyst declined. From the DRS and Mott–Schottky tests results, it can be known that as the zinc content increased, the photocatalyst sacrificed part of the visible light utilization rate, and at the same time, a more negative CB edge was obtained. The light-harvesting capacity and redox potential of a photocatalyst are crucial and significantly affect the photocatalytic hydrogen production activity [27, 38]. Here, when x < 0.3, the catalytic performance mainly depends on the redox ability of the photocatalyst; in contrast, when x > 0.3, the performance is mainly determined by the photocatalytic light absorption capacity. Properly adjusting the relative content of zinc and cadmium in the $Zn_xCd_{1-x}S$ solid solution, the light-harvesting ability and the redox potential
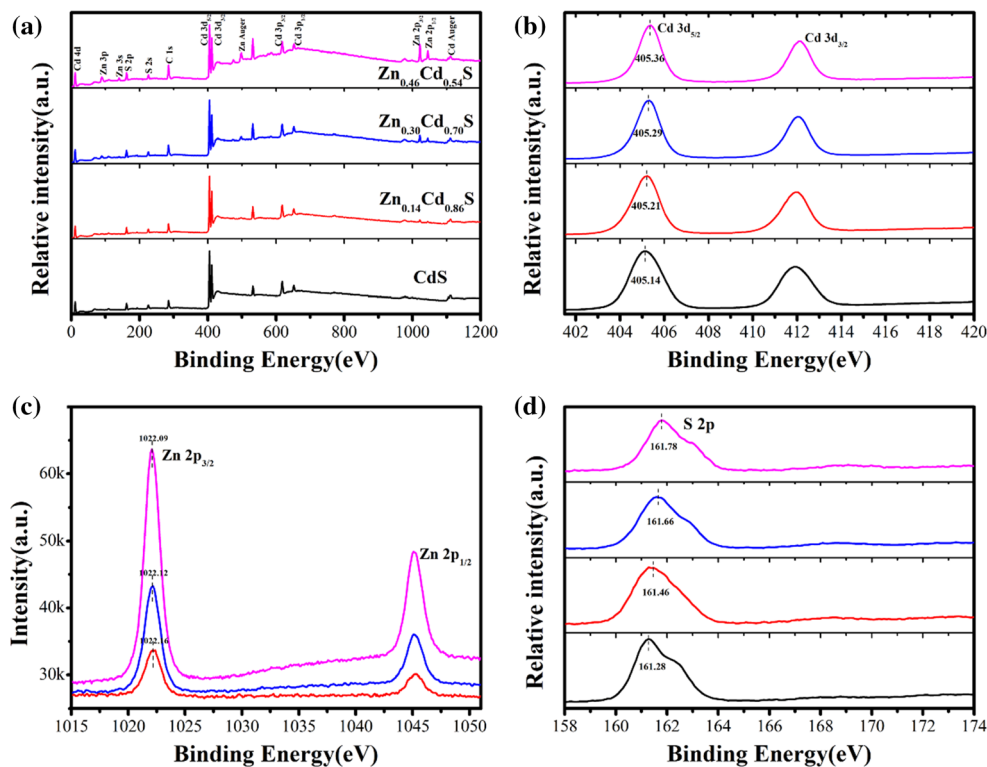
**Figure 5** **a** XPS full spectra and high-resolution XPS spectra of Cd 3d **b**, Zn 2p **c**, and S 2p **d** of $Zn_xCd_{1-x}S$ specimens with different metal contents.

have reached a good balance, which is the main reason why $Zn_{0.3}Cd_{0.7}S$ shows the best catalytic performance. The catalytic performances of $Zn_xCd_{1-x}S$-n samples are also given in Fig. 6b. The catalytic performance was similar to that of $Zn_xCd_{1-x}S$. It was worth noting that the catalytic performance of $Zn_{0.11}Cd_{0.89}S$-4 dropped significantly, even lower than that of CdS. This is because the size of the obtained $Zn_{0.11}Cd_{0.89}S$-4 sample increases significantly with the increase in the ammonia solution dosage.

The stability of the $Zn_{0.3}Cd_{0.7}S$ specimen was tested in the identical catalytic process. Figure 6c reveals the brilliant performance of the $Zn_{0.3}Cd_{0.7}S$ sample during the four cycles. After 16 h of irradiation, $Zn_{0.3-}Cd_{0.7}S$ specimen still maintained satisfactory hydrogen production performance. In addition, the catalyst after the cycle test was recovered and further characterized by XRD (Fig. 7a) and TEM (Fig. 7b). It was affirmed that the basic crystal structure and monodisperse spherical characteristics of $Zn_{0.3}Cd_{0.7}S$ were retained after four cycles. All the above phenomena have strongly proved the excellent

photocatalytic hydrogen production performance of $Zn_{0.3}Cd_{0.7}S$.

To further reveal the PEC properties of the synthetic $Zn_xCd_{1-x}S$ solid solutions, electrochemical impedance spectroscopy (EIS) and transient photocurrent response measurements were carried out. As depicted in Fig. 8a, EIS Nyquist plots, the arc radius of $Zn_{0.30}Cd_{0.70}S$ was smallest among all samples. Therefore, the as-obtained $Zn_{0.30}Cd_{0.70}S$ material had higher charge transfer efficiency and lower charge recombination possibility than other samples [30, 39]. This is because an appropriate amount of doped zinc in the CdS lattice can provide a suitable impurity level, so the excited electrons from the CdS valence band can be easily injected into the conduction band [40]. The photocurrent response of $Zn_xCd_{1-x}S$ specimens is given in Fig. 8b. These catalysts exhibited a very stable and strong photocurrent response to simulated solar radiation. When the incident light was shielded, the current density quickly decayed to near zero. Apparently, for $Zn_{0.30}Cd_{0.70}S$ sample, the observed photocurrent density was significantly higher than that of other samples, which indicated that there were more
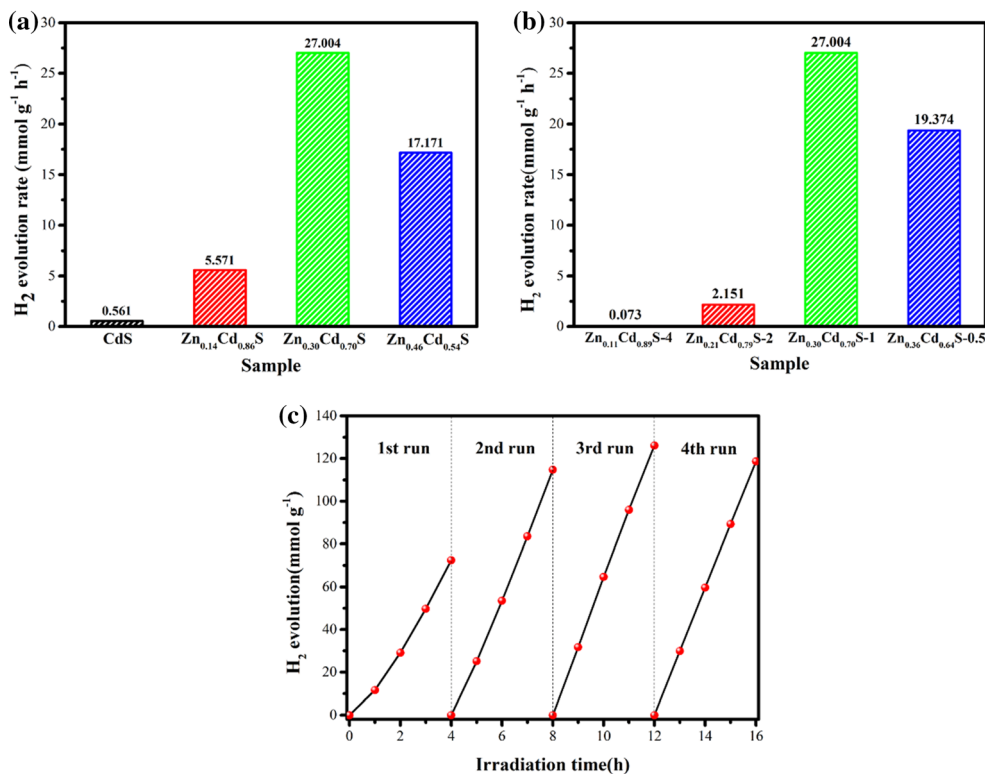
**Figure 6** **a** Photocatalytic $H_2$ evolution rate of $Zn_xCd_{1-x}S$ photocatalysts; **b** photocatalytic $H_2$ evolution rate of $Zn_xCd_{1-x}S$-n photocatalysts; **c** cycle tests of $Zn_{0.3}Cd_{0.7}S$ sample.
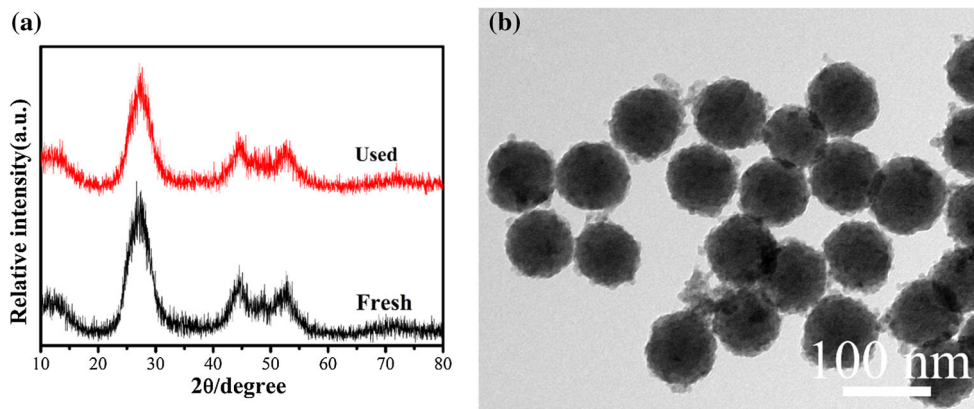


**Figure 7** **a** XRD patterns of $Zn_{0.30}Cd_{0.70}S$ photocatalyst before and after the cycle test for 16 h; **b** TEM image of $Zn_{0.30}Cd_{0.70}S$ photocatalyst after the cycle test.

separated photogenerated electrons and holes in the catalyst system. This can be attributed to the effective light utilization efficiency and fast photogenerated carrier mobility. It was worth noting that the decay trend of photocurrent and hydrogen production capability was synchronized. So, the improved photocatalytic hydrogen production performance should also be attributed to the improved photogenerated charge transfer capacity and elevated photocurrent.

Generally, an effective photocatalytic reaction involves three processes, including light harvesting, carrier generation and migration, and surface redox reaction. As shown in Fig. 9, the photocatalytic hydrogen production reaction occurring on $Zn_{0.30}$-$Cd_{0.70}S$ photocatalyst is revealed. Under the excitation of sunlight (the energy of this part of the incident photon is greater than or equal to the $E_g$ of the $Zn_{0.30}Cd_{0.70}S$), electrons are excited from VB and
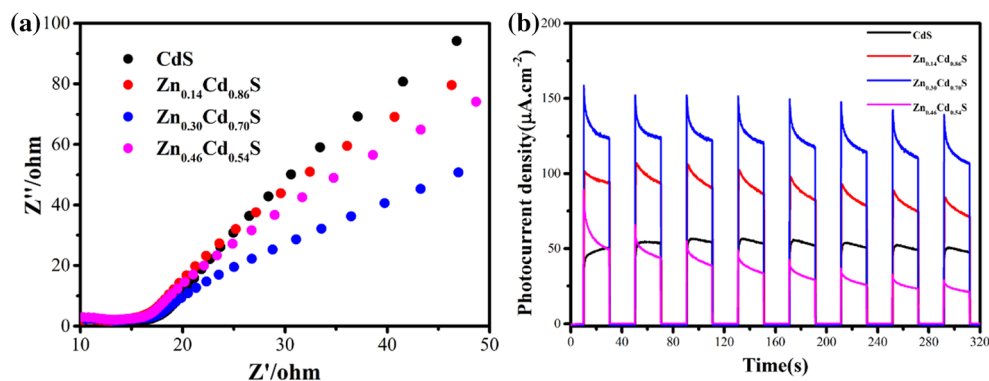
**Figure 8** **a** EIS Nyquist plots and **b** the transient photocurrent responses of the as-obtained $Zn_xCd_{1-x}S$ samples.

migrated to CB, generating negatively charged highly active electrons on the CB of the $Zn_{0.30}Cd_{0.70}S$, while leaving positively charged holes in the VB. Because there are a large number of sacrificial agents ($Na_2S$ and $Na_2SO_3$) with strong reducing ability in the catalytic reaction system, the photogenerated holes would be captured and consumed quickly. The photogenerated electrons could reach to the surface reaction site and undergo a reduction reaction with the adsorbed water to produce hydrogen. Although the $E_g$ of the $Zn_xCd_{1-x}S$ materials are broadened due to the insertion of Zn ions in the CdS structure, the visible light-harvesting capacity decreases. But at the same time, the obtained solid solution materials photogenerated carriers gain stronger redox ability, which is beneficial to the rapid progress of the

electron catalyzed hydrogen production reaction and the hole oxidation reaction. The rapid consumption of electron–hole pairs is also conducive to the regeneration of photogenerated carriers and the continuous and efficient progress of catalytic reactions. The rapid transport and transfer of carriers had also been confirmed by EIS and transient photocurrent tests. The best hydrogen production performance was obtained on $Zn_{0.30}Cd_{0.70}S$ sample, indicating that the improvement in photocatalytic performance benefits from the balance between light absorption and redox potential, as well as rapid carrier transfer and improved photocurrent response.

## Conclusions

In summary, by controlling the insertion of Zn into the CdS lattice, a series of monodisperse $Zn_xCd_{1-x}S$ nanospheres were successfully synthesized via a simple chemical bath co-precipitation route. Through various characterizations and testings, the as-prepared $Zn_{0.30}Cd_{0.70}S$ material exhibited the best water splitting activity with a maximum hydrogen evolution rate of 27.004 mmol $g^{-1}$ $h^{-1}$, which was about 47 times higher than that of pure CdS (0.561 mmol $g^{-1}$ $h^{-1}$). Moreover, the $Zn_{0.30}Cd_{0.70}S$ sample exhibited excellent catalytic stability under long-term light irradiation. This enhancing effect can owe to the balance between light absorption and redox potential caused by the incorporation of Zn in the solid solution. Interestingly, by adjusting the dosage of the ammonia solution, we found that the ammonia concentration during the reaction was positively correlated with the cadmium content, crystallinity and size of the obtained $Zn_xCd_{1-x}S$ solid
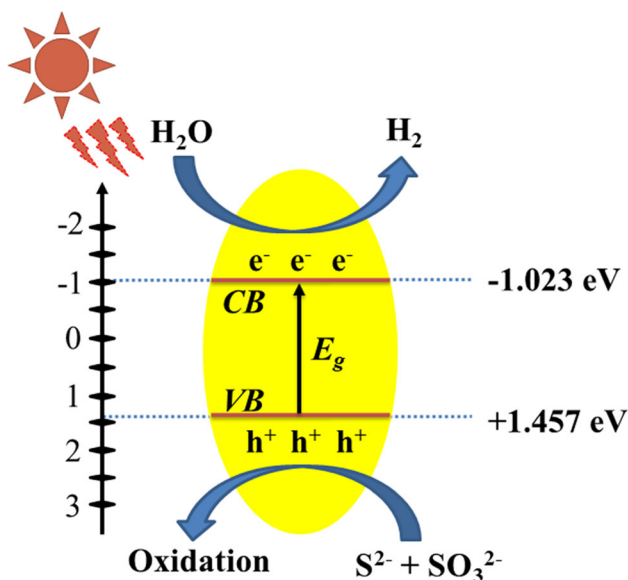


**Figure 9** Schematic diagram of the catalytic process performed on $Zn_{0.30}Cd_{0.70}S$ nanospheres.

solution samples. This work provides new possibilities for the simple preparation of $Zn_xCd_{1-x}S$ photocatalysis with high activity and stability and emphasizes the significant effect of ammonia on the formation of $Zn_xCd_{1-x}S$ solid solution.

## Acknowledgements

## Compliance with ethical standards

**Conflicts of interest** The authors declare that there is no conflict of interest.

## References

[1] Panwar NL, Kaushik SC, Kothari S (2011) Role of renewable energy sources in environmental protection: a review. Renew Sustain Energy Rev 15:1513–1524

[2] Zou X, Zhang Y (2015) Noble metal-free hydrogen evolution catalysts for water splitting. Chem Soc Rev 44:5148–5180

[3] Akira F, KENICHI H (1972) Electrochemical photolysis of water at a semiconductor electrode. Nature 238:37–38

[4.] Kudo A, Miseki Y (2009) Heterogeneous photocatalyst materials for water splitting. Chem Soc Rev 38:253–278

[5] Kang D, Kim TW, Kubota SR, Cardiel AC, Cha HG, Choi KS (2015) Electrochemical synthesis of photoelectrodes and catalysts for use in solar water splitting. Chem Rev 115:12839–12887

[6] Paracchino A, Laporte V, Sivula K, Gratzel M, Thimsen E (2011) Highly active oxide photocathode for photoelectrochemical water reduction. Nat Mater 10:456–461

[7] Ma Z, Hou H, Song K, Fang Z, Wang L, Gao F, Yang W, Tang B, Kuang Y (2020) Engineering oxygen vacancies by one-step growth of distributed homojunctions to enhance charge separation for efficient photoelectrochemical water splitting. Chem Eng J 379:22266

[8] Ng J, Xu S, Zhang X, Yang HY, Sun DD (2010) Hybridized nanowires and cubes: a novel architecture of a heterojunctioned TiO2/SrTiO3 thin film for efficient water splitting. Adv Func Mater 20:4287–4294

[9] Xu X, Liu G, Randorn C, Irvine JTS (2011) g-C3N4 coated SrTiO3 as an efficient photocatalyst for H2 production in aqueous solution under visible light irradiation. Int J Hydrogen Energy 36:13501–13507

[10] Zou J, Zhang L, Luo S, Leng L, Luo X, Zhang M, Luo Y, Guo G (2012) Preparation and photocatalytic activities of two new Zn-doped SrTiO3 and BaTiO3 photocatalysts for hydrogen production from water without cocatalysts loading. Int J Hydrogen Energy 37:17068–17077

[11] Zhong D, Liu W, Tan P, Zhu A, Liu Y, Xiong X, Pan J (2018) Insights into the synergy effect of anisotropic 001 and {230}facets of BaTiO 3 nanocubes sensitized with CdSe quantum dots for photocatalytic water reduction. Appl Catal B 227:1–12

[12] Han J, Liu Z, Guo K, Wang B, Zhang X, Hong T (2015) High-efficiency photoelectrochemical electrodes based on ZnIn2S4 sensitized ZnO nanotube arrays. Appl Catal B 163:179–188

[13] Ma D, Shi JW, Zou Y, Fan Z, Ji X, Niu C (2017) Highly efficient photocatalyst based on a CdS quantum dots/ZnO nanosheets 0D/2D heterojunction for hydrogen evolution from water splitting. ACS Appl Mater Interfaces 9:25377–25386

[14] Ma Y, Bian Y, Liu Y, Zhu A, Wu H, Cui H, Chu D, Pan J (2018) Construction of Z-scheme system for enhanced photocatalytic H2 evolution based on CdS quantum dots/CeO2 nanorods heterojunction. ACS Sustain Chem Eng 6:2552–2562

[15] Q. Qiao, K. Yang, L. Ma, W. Huang, B. Zhou, A. Pan, W. Hu, X. Fan, G. Huang, Facile in situ construction of mediator-free direct Z-scheme g-C3N4/CeO2 heterojunctions with highly efficient photocatalytic activity, Journal of Physics D: Applied Physics, 51 (2018).

[16] Zeng Y, Liu X, Liu C, Wang L, Xia Y, Zhang S, Luo S, Pei Y (2018) Scalable one-step production of porous oxygen-doped g-C3N4 nanorods with effective electron separation for excellent visible-light photocatalytic activity. Appl Catal B 224:1–9

[17] Xu Q, Cheng B, Yu J, Liu G (2017) Making co-condensed amorphous carbon/g-C3N4 composites with improved visible-light photocatalytic H2-production performance using Pt as cocatalyst. Carbon 118:241–249

[18] Y. Zhu, J. Li, J. Cao, C. Lv, G. Huang, G. Zhang, Y. Xu, S. Zhang, P. Meng, T. Zhan, D. Yang (2020). Phosphorus-doped polymeric carbon nitride nanosheets for enhanced photocatalytic hydrogen production. APL Materials. https://doi.org/10.1063/1.5143711

[19] Zhu B, Lin B, Zhou Y, Sun P, Yao Q, Chen Y, Gao B (2014) Enhanced photocatalytic H2 evolution on ZnS loaded with graphene and MoS2 nanosheets as cocatalysts. J Mater Chem A 2:3819–3827

[20] Hao X, Wang Y, Zhou J, Cui Z, Wang Y, Zou Z (2018) Zinc vacancy-promoted photocatalytic activity and photostability of ZnS for efficient visible-light-driven hydrogen evolution. Appl Catal B 221:302–311

[21] Jiang D, Sun Z, Jia H, Lu D, Du P (2016) A cocatalyst-free CdS nanorod/ZnS nanoparticle composite for high-performance visible-light-driven hydrogen production from water. J Mater Chem A 4:675–683

[22] Pareek A, Paik P, Borse PH (2016) Stable hydrogen generation from Ni- and Co-based co-catalysts in supported CdS PEC cell. Dalton Trans 45:11120–11128

[23] Tan P, Zhu A, Qiao L, Zeng W, Cui H, Pan J (2019) Manganese oxide at cadmium sulfide (MnOx@CdS) shells encapsulated with graphene: a spatially separated photocatalytic system towards superior hydrogen evolution. J Colloid Interface Sci 533:452–462

[24] Zhu C, Liu C, Zhou Y, Fu Y, Guo S, Li H, Zhao S, Huang H, Liu Y, Z, (2017) Kang, carbon dots enhance the stability of CdS for visible-light-driven overall water splitting. Appl Catal B: Environ 216:114–121

[25] Ning X, Li J, Yang B, Zhen W, Li Z, Tian B, Lu G (2017) Inhibition of photocorrosion of CdS via assembling with thin film TiO2 and removing formed oxygen by artificial gill for visible light overall water splitting. Appl Catal B 212:129–139

[26] Wu P, Liu Z, Guo Z, Li X, Zhao L (2019) Zn1−xCdxS nanowall photoanode prepared via seed layer epitaxial growth method and modified by dual co-catalyst for photo-electrochemical water splitting. Appl Surf Sci 467–468:65–74

[27] Li Q, Meng H, Zhou P, Zheng Y, Wang J, Yu J, Gong J (2013) Zn1–xCdxS solid solutions with controlled bandgap and enhanced visible-light photocatalytic H2-production activity. ACS Catal 3:882–889

[28] Zhong W, Huang X, Xu Y, Yu H (2018) One-step facile synthesis and high H2-evolution activity of suspensible CdxZn1-xS nanocrystal photocatalysts in a S(2-)/SO3(2-) system. Nanoscale 10:19418–19426

[29] Chen J, Chen J, Li Y (2017) Hollow ZnCdS dodecahedral cages for highly efficient visible-light-driven hydrogen generation. J Mater Chem A 5:24116–24125

[30] Zhang C, Liu H, Wang W, Qian H, Cheng S, Wang Y, Zha Z, Zhong Y, Hu Y (2018) Scalable fabrication of ZnxCd1-xS double-shell hollow nanospheres for highly efficient hydrogen production. Appl Catal B 239:309–316

[31] Xiang J, Wang H, Wang X, Chen X, Wu T, Wan H, Liu Y, Wang H (2019) Colloidal CdxZn1−xS nanocrystals as efficient photocatalysts for H2 production under visible-light irradiation. RSC Advances 9:4001–4007

[32] Yang B, Wang M, Hu X, Zhou T, Zang Z (2019) Highly efficient semitransparent CsPbIBr 2 perovskite solar cells via low-temperature processed In2S3 as electron-transport-layer. Nano Energy 57:718–727

[33] Yang M, Wang Y, Ren Y, Liu E, Fan J, Hu X (2018) Zn/Cd ratio-dependent synthetic conditions in ternary ZnCdS quantum dots. J Alloy Compd 752:260–266

[34] Wang DH, Wang L, Xu AW (2012) Room-temperature synthesis of Zn(0.80)Cd(0.20)S solid solution with a high visible-light photocatalytic activity for hydrogen evolution. Nanoscale 4:2046–2053

[35] Chen J, Ding B, Wang T, Li F, Zhang Y, Zhao Y, Qian H (2014) Facile synthesis of uniform ZnxCd1−xS alloyed hollow nanospheres for improved photocatalytic activities. J Mater Sci: Mater Electron 25:4103–4109. https://doi.org/10.1007/s10854-014-2135-4

[36] Boltersdorf J, Sullivan I, Shelton TL, Wu Z, Gray M, Zoellner B, Osterloh FE, Maggard PA (2016) Flux synthesis, optical and photocatalytic properties of n-type Sn2TiO4: hydrogen and oxygen evolution under visible light. Chem Mater 28:8876–8889

[37] L. Zhang, Y. Xue, S. Feng, Q. Guo (2019). Influence of ammonia concentration on the structural, composition and optical properties of CdZnS thin films. Mater Sci Semicond Process. https://doi.org/10.1016/j.mssp.2019.104650

[38] Zhao X, Feng J, Liu J, Shi W, Yang G, Wang GC, Cheng P (2018) An efficient, visible-light-driven, hydrogen evolution catalyst NiS/ZnxCd1-x S nanocrystal derived from a metal-organic framework. Angew Chem Int Ed Engl 57:9790–9794

[39] Qiu J, Zhang XF, Zhang X, Feng Y, Li Y, Yang L, Lu H, Yao J (2018) Constructing Cd0.5Zn0.5S@ZIF-8 nanocomposites

through self-assembly strategy to enhance Cr(VI) photocatalytic reduction. J Hazard Mater 349:234–241

[40] Huang J, Liu J, Han K (2012) Hybrid functionals studies of structural and electronic properties of ZnxCd(1–x)S and (ZnxCd1−x)(SexS1−x) solid solution photocatalysts. Int J Hydrogen Energy 37:17870–17881